eJSSNT Regular Paper

e-Journal of Surface Science and Nanotechnology **24**, 90–97 (2026)

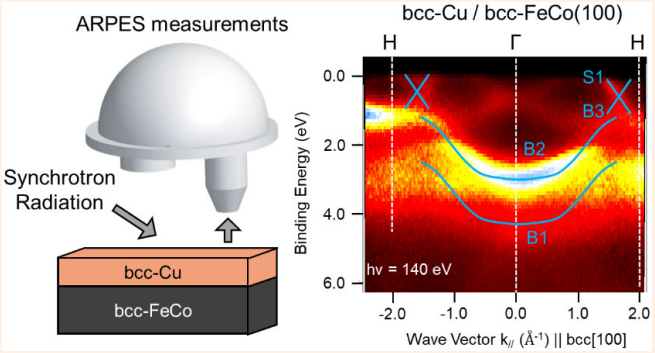
Electronic Structure of Metastable bcc-Cu Ultra-thin Films Grown on FeCo(100) Probed by Angle-resolved Photoemission Spectroscopy

Shingo Takezawa,[a, b] Daichi Ishikawa,[a, b] Soichi Takase,[a, b] Toshiro Osawa,[a, b] Riku Goto,[a, b] Arpita Varadwaj,[b] Kentaro Fuku,[c] Masaki Imamura,[d] Yukimi Tanimoto,[e] Hitoshi Sato,[f] Kiyohisa Tanaka,[g] Yuya Sakuraba,[b] Satoru Ichinokura,[b] Koichiro Yaji,[b, h] Masato Kotsugi,[a] Naoka Nagamura [a, b, i, †]

[a] *Department of Materials Science and Technology, Tokyo University of Science, Katsushika-ku, Tokyo 125-8585, Japan*
[b] *National Institute for Materials Science, Tsukuba, Ibaraki 305-0047, Japan*
[c] *Department of Chemistry, Graduate School of Science, Nagoya University, Nagoya, Aichi 464-8602, Japan*
[d] *Synchrotron Light Application Center, Saga University, Honjo, Saga 840-8502, Japan*
[e] *Graduate School of Advanced Science and Engineering, Hiroshima University, Higashi-Hiroshima, Hiroshima 739-8526, Japan*
[f] *Research Institute for Synchrotron Radiation Science, Hiroshima University, Higashi-Hiroshima, Hiroshima 739-0046, Japan*
[g] *UVSOR Facility, Institute for Molecular Science, Okazaki, Aichi 444-8585, Japan*
[h] *Unprecedented-scale Data Analytics Center, Tohoku University, Sendai, Miyagi 980-8578, Japan*
[i] *Research Institute of Electrical Communication, Tohoku University, Sendai, Miyagi 980-8577, Japan*
[†] *Corresponding author: NAGAMURA.Naoka@nims.go.jp*

Received: 11 March, 2026; Accepted: 14 July, 2026; J-STAGE Advance Publication: 5 September, 2026; Published: 5 September, 2026

We report an experimental investigation of the electronic band structure of metastable body-centered cubic (bcc)-Cu ultra-thin films epitaxially grown on FeCo(100) substrates. High-quality bcc-Cu films were fabricated by molecular beam epitaxy, enabling *in-situ* synchrotron angle-resolved photoemission spectroscopy measurements with sufficient energy and momentum resolution. The Fermi surface morphology of bcc-Cu was distinguished from that of conventional face-centered cubic-Cu and showed characteristic features consistent with the bcc structure. Overall, the experimentally observed band dispersions exhibit good qualitative agreement with density functional theory (DFT) calculations. However, the Cu-derived bands are systematically shifted toward higher binding energies compared to bulk-based DFT predictions. These deviations are likely caused by a combination of intrinsic limitations of the DFT approximation and interface-induced effects such as charge transfer at the Cu/FeCo heterointerface. The present results highlight the importance of experimentally determining the electronic structure of metastable ultra-thin films and demonstrate that interface effects must be considered when discussing Fermi surface matching and transport properties in Cu/FeCo heterostructures.



Keywords *Angle-resolved photoemission; Molecular beam epitaxy; Copper; Metastable states*

I. INTRODUCTION

The crystallographic growth of metallic thin films has long been a central topic in surface science [1]. As the film thickness is reduced to the nanometer scale, thin films increasingly exhibit low-dimensional characteristics, and their structural, electronic, and transport properties become strongly influenced by the underlying substrates. In such ultra-thin regimes, film growth is governed by a complex interplay of epitaxial strain, interfacial bonding, quantum-size effects, and growth parameters. Consequently, the resulting electronic structure often deviates from predictions based

on idealized bulk models obtained from density functional theory (DFT) calculations.

Copper (Cu) is one of the most ubiquitous metallic elements and is widely used in electronic devices as an interconnect material. In particular, FeCo/Cu/FeCo multilayer heterostructures have attracted considerable attention because they exhibit extremely large magnetoresistance (MR) ratios when employed as current-in-plane giant magnetoresistance (CIP-GMR) devices [2–4]. Previous studies have attributed this enhanced MR effect to strong spin-dependent scattering at the Cu/FeCo interfaces. The underlying mechanism has been interpreted in terms of Fermi surface matching, or electron band matching, in which the Fermi surface of the nonmagnetic Cu layer closely matches that of the majority-spin band of the ferromagnetic FeCo layer, while showing a significant mismatch with the minority-spin band [2, 5]. As a result, the Cu/FeCo interface is expected to act as an efficient spin filter, preferentially transmitting majority-spin electrons.

It has been reported that ultra-thin Cu layers grown on body-centered cubic (bcc)-FeCo(100) substrates by sputtering do not adopt the bulk-stable face-centered cubic (fcc) structure, but instead form a metastable bcc phase templated by the underlying FeCo lattice [2–4, 6, 7]. These findings highlight that the physical properties of Cu thin films in such heterostructures are strongly influenced by the substrate and may differ substantially from those of bulk Cu. Nevertheless, most theoretical discussions about electronic states of bcc-Cu, including Fermi surface matching at the bcc-Cu/FeCo interface, have been based on calculations assuming ideal bulk bcc-Cu [2, 5, 8], neglecting the effects of reduced dimensionality, epitaxial strain, and interfacial interaction inherent to ultra-thin films. Therefore, an experimental determination of the electronic structure of bcc-Cu in realistic Cu/FeCo heterostructures is essential for a quantitative evaluation of Fermi surface and electron band matching in actual devices.

Despite its importance, experimental investigations of the electronic structure of bcc-Cu remain scarce. Although DFT calculations have extensively explored the band structure of bulk bcc-Cu, previous angle-resolved photoemission spectroscopy (ARPES) studies on bcc-Cu films grown on Ag(100) [9] were limited by insufficient energy and momentum resolution. Moreover, the bcc-Cu films often contained substantial fractions of fcc domains and structural defects [9, 10] making it difficult to unambiguously identify the intrinsic electronic states of bcc-Cu. Because both Cu and FeCo surfaces are highly susceptible to oxidation, reliable ARPES measurements further require the preparation of large-area, structurally uniform films and *in-situ* spectroscopic characterization.

In our previous work, we demonstrated that high-quality, large-area bcc-Cu ultra-thin films can be fabricated on FeCo(100) substrates by molecular beam epitaxy (MBE), with minimal structural disorder and negligible fcc-Cu contamination [11]. Building on this growth technique, the present study reports high-resolution *in-situ* synchrotron ARPES measurements of the electronic structure of bcc-Cu epitaxially grown on FeCo(100). By combining multi-photon-energy ARPES with first-principles calculations, we experimentally determine the band dispersions and Fermi surface morphology of bcc-Cu in this heterostructure and quantitatively assess their deviations from bulk DFT predictions. These results provide essential insight into the electronic structure of metastable bcc-Cu ultra-thin films and an experimental foundation for evaluating Fermi surface matching at Cu/FeCo interfaces in spintronic devices.

II. EXPERIMENTAL

FeCo and Cu thin films were grown on MgO(100) substrates by MBE in an ultra-high vacuum (UHV) system with a base pressure of ~9×10^{-8} Pa. MgO(100) substrates were annealed at 800 K for 30 min prior to deposition to obtain clean and well-ordered surfaces. The evaporation sources were a high-purity $Fe_{0.5}Co_{0.5}$ rod (TOSHIMA Manufacturing, $2 \times 2 \times 20$ mm, 4N) and a Cu wire (Nilaco, 0.25 mm diameter, 5N). The surface crystallinity and structural phase of the FeCo layers and Cu overlayers were examined by *in-situ* low-energy electron diffraction (LEED).

FeCo layers were first deposited on MgO(100) substrates and served as the structural and electronic template for the subsequent growth of Cu overlayers. FeCo films were grown using an electron-beam (EB) evaporator with the emission current fixed at 20 mA, while maintaining the substrate temperature at 600 K. The FeCo film thickness was confirmed *ex-situ* by X-ray reflectivity (XRR) measurements using a laboratory-based X-ray diffractometer (Rigaku SmartLab), performed after the ARPES experiments, and a thickness of at least 20 nm was verified for all samples prepared at each synchrotron facility. The thickness was chosen to ensure bulk-like electronic properties of the FeCo layer.

After the growth of FeCo, Cu overlayers were deposited at room temperature using an EB evaporator with the emission current fixed at 30 mA. In our previous studies, Cu films grown on FeCo(100) were shown to exhibit a bcc structure only in the ultra-thin regime below approximately 1 nm, whereas thicker films relaxed toward the bulk-stable fcc phase [11]. Consistent with this thickness-dependent structural transition, the bcc nature of the present Cu overlayers was verified by *in-situ* LEED *I-V* analysis over an incident electron-energy range of 150–400 eV. Accordingly, the nominal thickness of the Cu layers in the present study was below 1 nm. The presence of Cu in the overlayer was further confirmed by laboratory-based *in-situ* X-ray photoelectron spectroscopy (XPS) measurements performed on reference samples prepared under identical growth conditions. The XPS measurements were carried out using a VG Scienta SES-100 hemispherical analyzer with an Al Kα radiation source ($h\nu$ = 1486.6 eV).

ARPES measurements were carried out at three synchrotron radiation facilities: the BL-7 beamline of HiSOR, the BL13 beamline of SAGA-LS [12], and the BL7U beamline of UVSOR [13, 14]. The photon-energy ranges used were 30–400, 45–180, and 12–38 eV at HiSOR, SAGA-LS, and

UVSOR, respectively. The total energy resolution was set to approximately 130 meV ($h\nu$ = 140 eV), 75 meV ($h\nu$ = 140 eV), and 38 meV ($h\nu$ = 38 eV), at HiSOR, SAGA-LS, and UVSOR, respectively. The angular resolution was about 0.1° at all endstations. Linearly polarized light with horizontal polarization was used in all ARPES measurements. During data acquisition, the pressure in the measurement chambers was maintained below 1×10^{-8} Pa, and the sample temperature was kept below 20 K. All beamlines were equipped with UHV preparation chambers and LEED optics directly connected to the ARPES measurement chambers, allowing the as-grown samples to be transferred and measured *in-situ* without exposure to air. The binding-energy scale was calibrated using the Fermi edge of each sample and cross-checked with reference measurements on a gold surface.

First-principles calculations of the electronic band structure of bcc-Cu and bcc-FeCo were performed within DFT using the Vienna *Ab initio* Simulation Package (VASP) [15]. The exchange-correlation functional was treated within the semi-local generalized gradient approximation (GGA-PBE), employing a $20 \times 20 \times 20$ Monkhorst-Pack k-point mesh. Spin polarization was included, and both the lattice parameters and magnetic moments were allowed to relax. The bcc-FeCo alloy was modeled using the virtual crystal approximation (VCA) [16], where Fe sites were replaced by an effective potential corresponding to 50 % Co substitution, yielding an $Fe_{0.5}Co_{0.5}$ potential. Such interpolation approaches have been widely adopted and shown to provide reliable descriptions of electronic structures in substitutional alloys [17–21]. Additional slab calculations were also carried out to estimate the work functions of bcc-Cu(100) and FeCo(100), and to visualize the charge-density redistribution at the bcc-Cu(100)/FeCo(100) interface. Details of the slab models, structural relaxation, vacuum thickness, dipole correction, and charge-density-difference analysis are described in Supplementary Material.

III. RESULTS AND DISCUSSIONS

Figure 1(a, b) shows the LEED patterns of clean FeCo(100) and Cu/FeCo(100) recorded at the same sample–screen distance. Under this identical geometry, the spacing between diffraction spots directly reflects the in-plane atomic periodicity of the surface. The in-plane atomic spacing of fcc Cu (2.5 Å) is smaller than that of bcc FeCo and metastable bcc Cu (2.9 Å), which is confirmed in Figure S1 in Supplemental Material. No additional spots corresponding to an fcc lattice are observed in Figure 1(b), indicating the absence of the fcc-Cu phase under the present growth conditions. The bcc character of the LEED patterns is further supported by the incident-electron-energy dependence of the 01 diffraction spot in the LEED *I-V* measurements [11].

Figure 1(c, d) shows XPS spectra acquired from a sample prepared in a laboratory-based system following essentially the same deposition process as that for the ARPES measurements, confirming the presence of Cu at the sample surface.

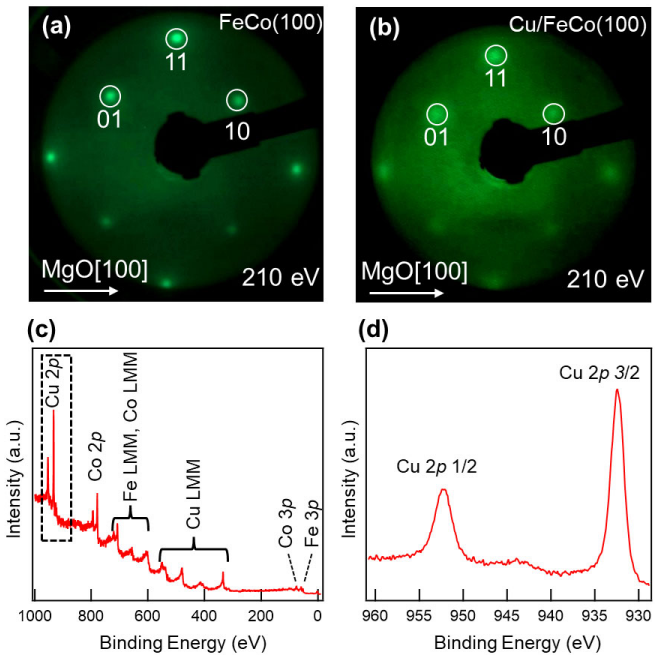


Figure 1: Representative LEED patterns of (a) a clean FeCo(100) surface and (b) a Cu/FeCo(100) surface recorded under the same sample–screen geometry at UHV preparation chambers in synchrotron radiation facilities. (c, d) XPS spectrum of Cu/FeCo(100): a wide-scan spectrum (c) and an enlarged view of the Cu core-level region (d) on reference samples taken at a UHV preparation chamber in laboratory-based system, confirming the presence of Cu at the sample surface.

As the surface energy of Cu is lower than that of both Fe(100) and Co(100) [22–24], Cu is expected to wet the FeCo(100) surface, suggesting that the substrate is uniformly covered by the Cu overlayer. Moreover, previous transmission electron microscopy studies have reported that no significant atomic interdiffusion occurs at the Cu/FeCo interface [4, 11]. These observations indicate that a bcc-Cu(100) thin film is formed on a sufficiently relaxed FeCo(100) surface under the present growth conditions.

Figure 2 presents ARPES intensity maps measured along the Γ–N direction at SAGA-LS, together with the corresponding second-derivative plots and the DFT-calculated band structures. The raw ARPES intensity maps shown in Figure 2(a, b) exhibit intensity variations depending on emission angle, mainly due to instrumental response and matrix-element effects. Since such intensity modulations make it difficult to directly evaluate weak dispersive features from the raw maps alone, second-derivative maps are also shown in Figure 2(c, d) to enhance the visibility of the band dispersions. For the clean FeCo(100) substrate [Figure 2(a)], a parabolic band (dashed line) is observed at binding energies E_B = 2.0–3.0 eV. This feature is also clearly identified in the corresponding second-derivative map [Figure 2(c)]. After Cu deposition, an additional parabolic band appears at E_B = 4.0–5.0 eV, as shown in Figure 2(b) (solid line), which is absent in the spectrum of the clean FeCo(100) surface. This additional band is more clearly resolved in the second-derivative

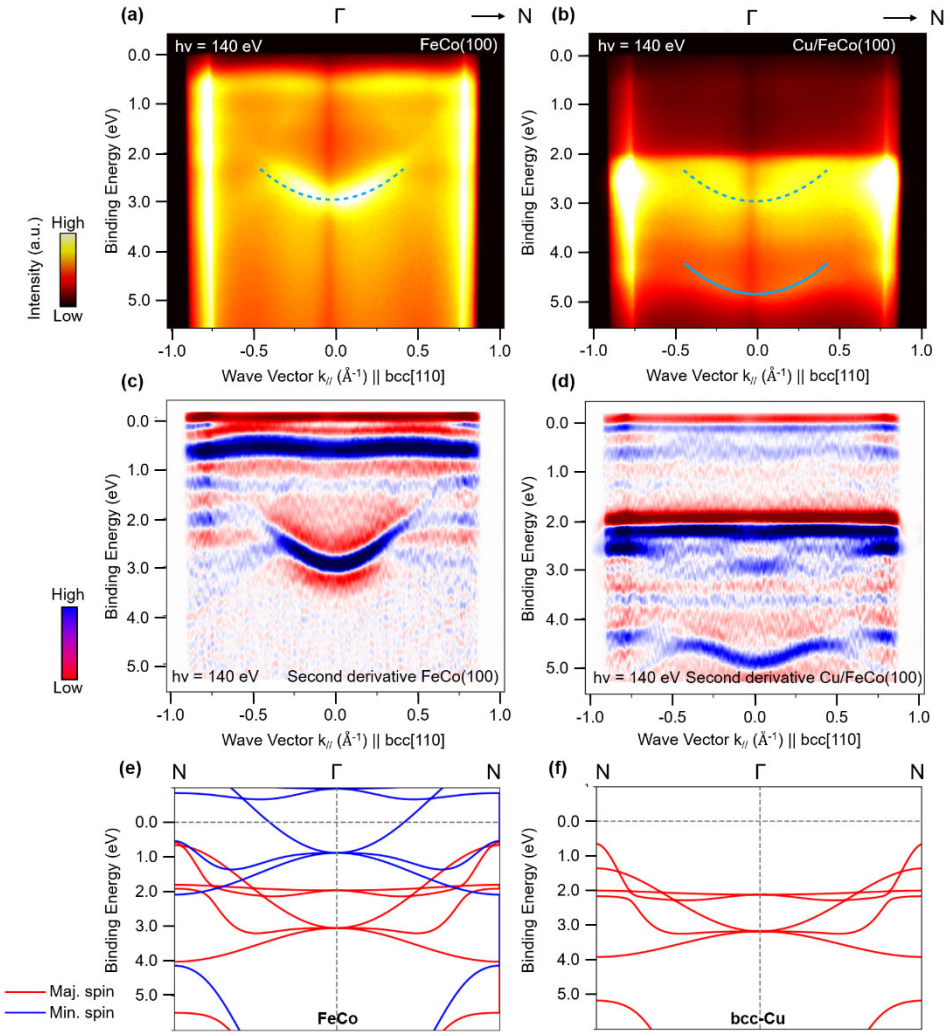


Figure 2: (a, b) ARPES intensity maps of (a) FeCo(100) and (b) bcc-Cu/FeCo(100) as a function of $k_{//}$ and E_B measured along the Γ–N line with $h\nu = 140$ eV, respectively. (c, d) The corresponding second derivative plots of (c) FeCo(100) and (d) bcc-Cu/FeCo(100). (e, f) The DFT-calculated band structure of (e) FeCo and (f) bcc-Cu.

map [Figure 2(d)]. As this band exhibits clear dispersive behavior and appears only after Cu deposition, it is reasonable to assign it to bcc-Cu, although the presence of a minor amorphous Cu component cannot be completely excluded. The parabolic band originating from the FeCo substrate (dashed line), which is also visible in Figure 2(a), remains observable even after Cu deposition because the thickness of the Cu overlayer is sufficiently small compared with the probing depth of the present ARPES measurement ($h\nu = 140$ eV) [25]. In addition, the photoemission intensity in the binding-energy range of $E_B = 0.0$–2.0 eV is reduced after Cu deposition. This behavior can be attributed to the difference in the electronic configurations of FeCo and Cu. In FeCo, partially occupied 3d states extend up to the vicinity of the Fermi level, resulting in high-photoemission intensity at $E_B < 2.0$ eV. In contrast, for Cu, the 3d states are fully occupied in both the bcc and fcc phases located at higher binding energies by stabilization of the 3d electrons. As a result, the photoemission intensity near E_F is significantly reduced after Cu deposition. A similar reduction of near E_F intensity is also observed for thicker fcc-Cu films (see Figure S1 in Supplementary Material). Therefore, the dispersive band observed at higher binding energies than the bcc-FeCo-derived band is attributed to bcc-Cu.

Figure 3 shows Fermi surface mappings of Cu/FeCo(100) obtained by ARPES experiments at HiSOR BL-7, together with the corresponding DFT-calculated Fermi surfaces. From the periodicity of the $k_{\perp}$–$k_{//}$ mapping in Figure 3(c), the inner potential V_0 was experimentally estimated to be $V_0 = 31$ eV, and a photon energy of $h\nu = 140$ eV corresponds to the Γ point. The Fermi surface mapping in Figure 3(c) was measured in an experimental geometry where the in-plane momentum axis was aligned parallel to the bulk MgO[110] direction. Previous works [2, 11] established the epitaxial relationship MgO[110] || bcc[100] || fcc-Cu[110] in Cu/FeCo/MgO(100) heterostructures. Accordingly, under the assumption of a bcc-Cu lattice, the present geometry probes the Γ–H–N plane of the bcc Brillouin zone [Figure 3(a)]. In contrast, if fcc-Cu is assumed, the measurement corresponds to the Γ–K–X plane of the fcc Brillouin zone [Figure 3(b)].

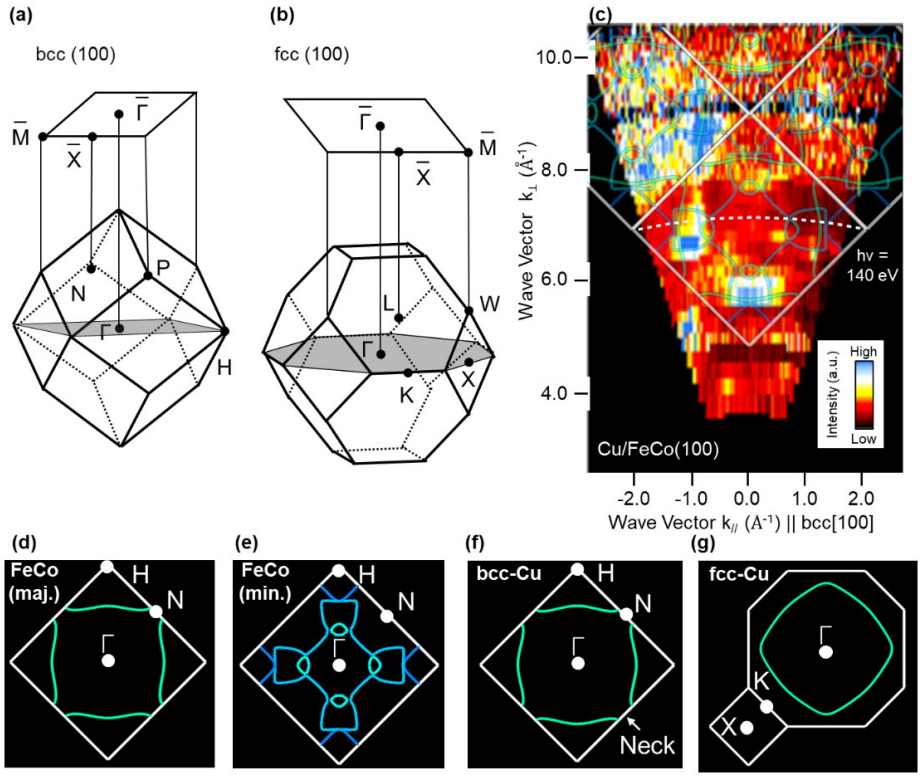


Figure 3: The three-dimensional first Brillouin zones and the two-dimensional projection of (a) bcc lattice, and (b) fcc lattice, respectively. (c) Photon-energy-dependent ARPES constant-energy surface in the $k_{\perp}$–$k_{//}$ plane of Cu/FeCo(100) at the Fermi level ($h\nu$ = 30–400 eV), overlaid by (d–f), showing the bcc-like neck structure. (d–g) DFT-calculated Fermi surfaces of (d) majority-spin of bcc-FeCo, (e) minority-spin of bcc-FeCo, (f) bcc-Cu, at the cross section indicated in (a), and (g) fcc-Cu, at the cross section indicated in (b).

Figure 3(d–g) present bulk-band DFT calculations corresponding to these Brillouin-zone cuts for bcc-FeCo [Figure 3(d, e)], bcc-Cu [Figure 3(f)], and fcc-Cu [Figure 3(g)] at Fermi level. Because the photon-energy range used here (30–400 eV) yield an inelastic mean free path of approximately 1 nm [25], comparable to the Cu film thickness, the detected photoelectrons originate not only from the Cu overlayer but also from the underlying FeCo layer. Thus, the measured ARPES intensity in Figure 3(c) should not be interpreted as a fully Cu-derived Fermi surface, but rather as a superposition of spectral weight from the Cu/FeCo heterostructure.

Despite this overlap, the experimentally observed Fermi-surface morphology is clearly inconsistent with the neckless Fermi surface expected for conventional fcc-Cu [Figure 3(g)]. In particular, no significant spectral intensity is observed between the Γ and N points in the central Brillouin zone, whereas such intensity would be expected for the fcc-Cu Fermi surface in the corresponding Γ–K–X plane. The presence of a neck along the [100] direction in bcc-Cu is also consistent with earlier positron-annihilation measurements [26]. In addition, weak spectral weight observed near the Γ point of the first Brillouin zone can be attributed to the minority-spin component of the FeCo substrate. The Fermi surface observed in Figure 3(c) appears broadened. The origin of this broadening will be discussed in a later section.

Thus, although the finite momentum resolution and the coexistence of Cu- and FeCo-derived photoemission signals prevent a fully quantitative determination of the detailed Fermi-surface morphology, the data in Figure 3 support the formation of a bcc-type Cu electronic structure and show no indication of the neckless Fermi-surface morphology characteristic of fcc-Cu.

Figure 4(a) shows the ARPES intensity map of the Cu/FeCo along the Γ-H direction at a photon energy of $h\nu$ = 140 eV, which was measured at HiSOR BL-7, together with the corresponding energy distribution curves (EDCs) shown in Figure 4(b). The ARPES intensity map of Figure 4(a) was normalized so that the integrated intensity of each spectrum is identical. In the binding-energy range from 1.0 to 4.0 eV, two dispersive bands [B1 and B2 in Figure 4(a)] are clearly observed, both exhibiting a monotonic upward dispersion from Γ toward H. Based on the comparison of the Γ–N band dispersions in Figure 2, the deeper band (B1) is attributed to Cu-derived states, while the shallower one (B2) is assigned to FeCo-derived states.

The corresponding DFT band structures for FeCo and bcc-Cu are shown in Figure 4(c, d). Along the Γ–H direction, both systems exhibit Δ_5 bands with predominantly d-orbital character: a Δ_5 band for Cu and a majority-spin Δ_5 band for FeCo. The experimentally observed bands marked as B1 and B2 in Figure 4 are therefore attributed to these Δ_5 states. In addition, the bands observed near the Γ point at $E_B < 1$ eV are assigned to the minority-spin Δ_1 and Δ_5 band of FeCo, in

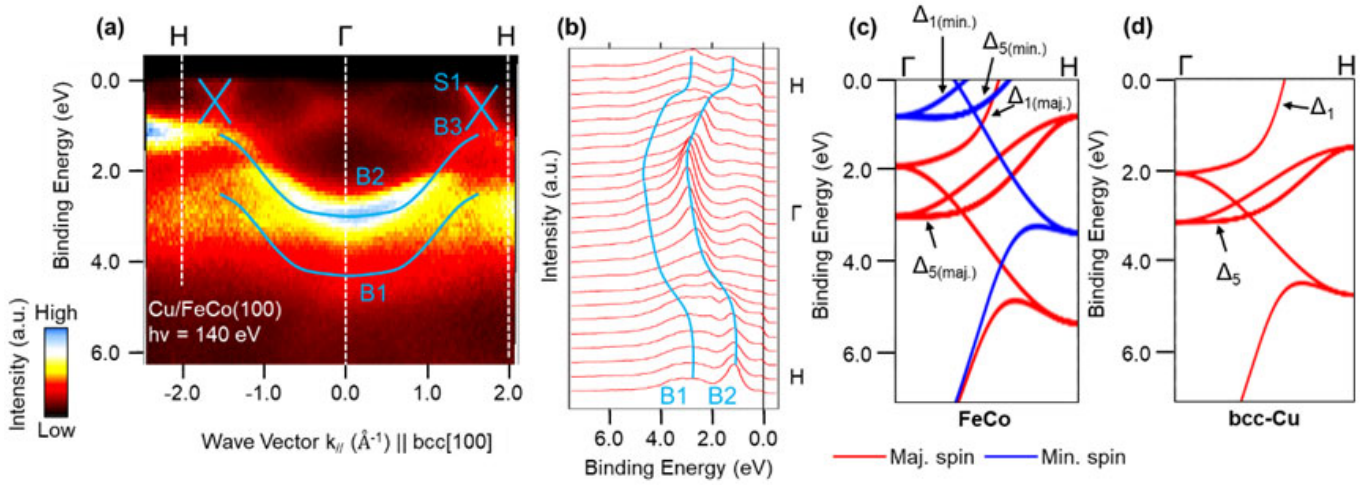


Figure 4: (a) ARPES intensity map of Cu/FeCo(100) as a function of $k_{//}$ and E_B along Γ–H line with $h\nu$ = 140 eV. (b) Energy-distribution curves from (a). (c) DFT-calculated band structure of FeCo (majority/minority). (d) DFT-calculated band structure of bcc-Cu.

good agreement with the DFT calculations.

Near the H point, two bands crossing the Fermi level (B3, S1) are observed. The band showing an upward dispersion from Γ to H (B3) is attributed to the Cu-derived Δ_1 band with predominantly s–p character. In contrast, the other band (S1) cannot be uniquely assigned to any bulk band predicted by the DFT calculations. Moreover, this feature shows no noticeable photon-energy dependence, suggesting that it is not a simple bulk-derived state. Possible origins include surface-related states, as reported for fcc-Cu surfaces, or quantum-well states (QWS) appearing away from the surface normal due to umklapp scattering [27–29]. The S1 feature is located close to the Fermi level and exhibits an apparently linear dispersion. Therefore, although its microscopic origin remains unclear, it may represent an electronic state with a relatively small effective mass or high group velocity, which could influence carrier transport in bcc-Cu/FeCo heterostructures. A detailed identification of this band, however, requires further experimental investigation.

One possible approach is systematic thickness-dependent ARPES measurements. Previous studies on QWS in fcc-Cu/Co(100) demonstrated that Cu thicknesses in the range of approximately 1–10 ML are sufficient to clarify the QWS character [30]. Considering the lattice constant of bcc-Cu, 10 ML is equivalent to a thickness of less than 2 nm. In addition, metastable bcc-Cu layers with thickness up to 2 nm have been realized in FeCo/bcc-Cu/FeCo multilayer structures [2]. Therefore, although experimentally demanding, monolayer-scale thickness-dependent ARPES measurements should be feasible in principle within the thickness range where the metastable bcc-Cu structure is preserved. Such measurements will be important for clarifying whether S1 originates from a QWS.

Although the overall qualitative behavior of the experimentally observed band dispersions is well reproduced by the DFT calculations, a pronounced quantitative discrepancy is found in the energy positions of the Cu-derived bands. In particular, the Cu-derived Δ_5 band is observed at a binding energy deeper by approximately 1.0 eV than predicted by bulk-based DFT calculations. A similar tendency is also found for the Δ_1 band, which crosses the Fermi level closer to the H point than expected from the calculations. Overall, the Cu-derived bands are systematically shifted toward higher binding energies compared to the DFT results.

Such band shifts directly modify the Fermi surface morphology, indicating that interfacial transport properties cannot be fully understood solely on the basis of Fermi surface matching arguments derived from ideal bulk DFT calculations. Several factors may contribute to the observed discrepancy between experiment and theory. First, it may partially originate from the intrinsic limitations of the DFT approximation employed. In particular, the GGA-PBE functional is known to suffer from self-interaction errors, which can lead to systematic shifts in band energies [31, 32]. Second, interface-induced charge redistribution may also play an important role. When two materials with different work functions form a heterointerface, charge redistribution occurs near the interface to align their Fermi levels. To examine this effect, additional slab calculations were performed for bcc-Cu(100), FeCo(100), and the bcc-Cu(100)/FeCo(100) interface. The calculated work functions were 4.395 eV for bcc-Cu(100) and 3.869 eV for FeCo(100), indicating a clear work-function difference between the two materials. Figure 5 shows the calculated charge-density-difference distribution at the bcc-Cu(100)/FeCo(100) interface. Enhanced electron density is observed on the bcc-Cu side near the interface, indicating electron transfer from FeCo to bcc-Cu and the occurrence of interfacial electron reconstruction. These results support the presence of interface-induced charge redistribution and local electrostatic potential modification in the bcc-Cu/FeCo heterostructure. This charge redistribution is consistent with the direction of the experimentally observed shift of the bcc-Cu-derived bands toward higher binding energy in the ARPES measurements. However, the magnitude of the observed shift

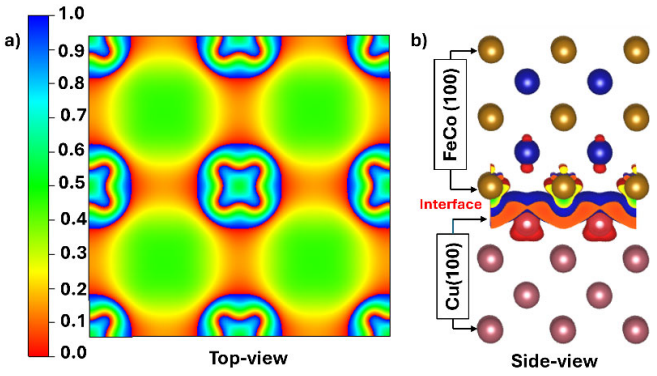


Figure 5: Charge-density-difference distribution at the bcc-Cu(100)/FeCo(100) interface calculated by DFT. (a) Top-view two-dimensional slice of the charge-density-difference distribution on a plane parallel to the interface. (b) Side-view three-dimensional charge-density-difference iso-surfaces. The charge-density difference was evaluated as $\Delta\rho = \rho$(interface) $- \rho$(bcc-Cu slab) $- \rho$(FeCo slab), where the isolated slab charge densities were calculated using the same atomic positions and lattice parameters as those in the interface model. In panel (a), the color map represents the charge-density difference on the selected plane. In panel (b), red and blue iso-surfaces indicate charge depletion and charge accumulation, respectively. The iso-surface value in panel (b) is ± 0.003 e Å^{-3}.

is likely influenced by multiple factors, including reduced screening in the ultrathin Cu layer, epitaxial strain, quantum-size effects, and limitations of the bulk-based DFT calculations.

Recent studies about the MR ratio of Cu/Fe$_\beta$Co$_{1-\beta}$ with varying compositions [5] revealed a small but systematic deviation between theoretical predictions and experimental results, suggesting that idealized bulk electronic structures do not fully capture the electronic states relevant to transport in realistic heterostructures. Our observation of interface-induced band shifts in bcc-Cu/FeCo suggests that such deviations can arise from modifications of the electronic structure at heterointerfaces.

These results indicate that, in realistic heterostructures, the electronic bands can be significantly modified from their ideal bulk counterparts, and that such modifications can be directly probed by ARPES. The present observations thus highlight the importance of considering interface-induced band shifts when discussing the electronic structure and transport properties of Cu/FeCo heterojunctions.

In the present study, the ability to grow high-quality bcc-Cu ultra-thin films by MBE on FeCo(100) substrates enabled direct ARPES observation of the bcc-Cu band dispersions. This experimental access reveals not only the characteristic Fermi surface morphology of bcc-Cu but also significant deviations from bulk-based DFT predictions, highlighting the importance of experimentally determining the electronic structure of metastable phases realized under epitaxial constraints.

IV. CONCLUSION

In summary, the electronic band structure of metastable bcc-Cu has been experimentally determined by combining our MBE growth technique with *in-situ* ARPES measurements. The Fermi surface morphology of bcc-Cu was clearly distinguished from that of conventional fcc-Cu, demonstrating the unique electronic structure of this metastable phase. This achievement provides a long-sought experimental benchmark for bcc-Cu, which has previously been discussed primarily on the basis of theoretical calculations.

Overall, the experimentally observed band dispersions show good qualitative agreement with DFT calculations. However, for bcc-Cu grown on FeCo, the Cu-derived electronic bands are systematically shifted toward higher binding energies compared to predictions based on ideal bulk DFT calculations. This discrepancy is likely caused not only by intrinsic limitations of the DFT approximation but also by interface-induced effects such as charge transfer at the Cu/FeCo interface.

These findings indicate that, in ultra-thin heterostructures, environmental effects such as interface formation play a crucial role in determining the electronic structure. Consequently, device performance predictions based solely on idealized bulk electronic structures, such as Fermi surface matching arguments, may be insufficient. Direct experimental determination of electronic states is therefore essential. In this context, future studies employing high-throughput ARPES measurement techniques, are expected to enable more reliable discussions of interface transport properties based on experimentally determined Fermi surfaces.

Acknowledgments

The authors thank Dr. Shunsuke Tsuda and Dr. Fumio Komori for fruitful discussions. We also thank Ms. Sanae Kuramochi, Ms. Natsuko Kojima and Mr. Fumiya Arai for technical supports. The synchrotron radiation experiments were performed with the approval of UVSOR (Proposal Number: 25IMS6667), SL-Center, Saga University (Proposal Numbers: R6-102V, R6-103V) and HiSOR (Proposal Number: 24BU002). This work is particularly supported by JST CREST (Grant Numbers: JPMJCR21O1, JPMJCR21O4), JST PRESTO, Japan (Grant Numbers: JPMJPR17NB, JPMJPR20T7), JSPS/MEXT KAKENHI (Grant Numbers: 25K01628, 24K01243, 24K01352, 21H01638, 21H04696, 25H00743), the Innovative Science and Technology Initiative for Security, ATLA (Grant Number: JPJ004596), the Cooperative Research Project Program of the Research Institute of Electrical Communication, Tohoku University, and JST SPRING (Grant Number: JPMJSP2151). The computation was performed using supercomputing facilities of Research Center for Computational Science, Okazaki, Japan (Project: 26-IMS-C337).

Appendix

The additional LEED patterns, corresponding ARPES intensity maps, and DFT calculation conditions are available in Supplementary Material at https://doi.org/10.1380/ejssnt.2026-014.

References

[1] N. Kaiser, Appl. Opt. **41**, 3053 (2002).
[2] K. B. Fathoni, Y. Sakuraba, T. Sasaki, Y. Miura, J. W. Jung, T. Nakatani, and K. Hono, APL Mater. **7**, 111106 (2019).
[3] D. Taparia, K. B. Fathoni, P. D. Kulkarni, A. Srinvasan, P. Alagarsamy, Y. Sakuraba, T. Nakatani, and K. Hono, J. Magn. Magn. Mater. **538**, 168321 (2021).
[4] K. B. Fathoni, Z. Li, T. Nakatani, Y. Sakuraba, T. Sasaki, and K. Hono, J. Magn. Magn. Mater. **551**, 169154 (2022).
[5] V. K. Kushwaha, R. Toyama, Y. Miura, Y. Iwasaki, and Y. Sakuraba, AIP Adv. **14**, 125329 (2024).
[6] H. Nakayama, B. Xu, S. Iwamoto, K. Yamamoto, R. Iguchi, A. Miura, T. Hirai, Y. Miura, Y. Sakuraba, J. Shiomi, and K. Uchida, Appl. Phys. Lett. **118**, 042409 (2021).
[7] F. Makino, T. Hirai, T. Shiga, H. Suto, H. Fujihisa, K. Oyanagi, S. Kobayashi, T. Sasaki, T. Yagi, K. Uchida, and Y. Sakuraba, Phys. Rev. B **112**, 054407 (2025).
[8] Z. Tang, M. Hasegawa, Y. Nagai, and M. Saito, Phys. Rev. B **65**, 195108 (2002).
[9] H. Li, D. Tian, J. Quinn, Y. S. Li, F. Jona, and P. M. Marcus, Phys. Rev. B **43**, 6342 (1991).
[10] Z. Q. Wang, S. H. Lu, Y. S. Li, F. Jona, and P. M. Marcus, Phys. Rev. B **35**, 9322(R) (1987).
[11] S. Takezawa, M. Riva, F. Dörr, M. Schmid, T. Sasaki, T. Hiroto, M. Kotsugi, K. Yaji, Y. Sakuraba, and N. Nagamura, e-J. Surf. Sci. Nanotechnol. **24**, 21 (2026).
[12] K. Takahashi, M. Imamura, I. Yamamoto, J. Azuma, K. Ogawa, M. Kamada, H. Ohkuma, and S. Yamamoto, J. Phys.: Conf. Ser. **425**, 072007 (2013).
[13] S. Kimura, T. Ito, M. Sakai, E. Nakamura, N. Kondo, T. Horigome, K. Hayashi, M. Hosaka, M. Katoh, T. Goto, T. Ejima, and K. Soda, Rev. Sci. Instrum. **81**, 053104 (2010).
[14] H. Ota, E. Salehi, M. Fujimoto, K. Hayashi, T. Horigome, H. Iwayama, M. Katoh, N. Kondo, S. Makita, F. Matsui, H. Matsuda, T. Mizukawa, A. Minakuchi, E. Nakamura, M. Nagasaka, Y. Okano, T. Ohigashi, M. Sakai, K. Sugita, K. Tanaka, Y. Taira, F. Teshima, J. Yamazaki, T. Yano, H. Yuzawa, and S. Kera, J. Phys.: Conf. Ser. **2380**, 012003 (2022).
[15] G. Kresse and J. Furthmüller, Phys. Rev. B **54**, 11169 (1996).
[16] C. Eckhardt, K. Hummer, and G. Kresse, Phys. Rev. B **89**, 165201 (2014).
[17] W. E. Pickett and D. J. Singh, Phys. Rev. B **53**, 1146 (1996).
[18] D. A. Papaconstantopoulos and W. E. Pickett, Phys. Rev. B **57**, 12751 (1998).
[19] A. M. Saitta, S. de Gironcoli, and S. Baroni, Phys. Rev. Lett. **80**, 4939 (1998).
[20] N. Marzari, S. de Gironcoli, and S. Baroni, Phys. Rev. Lett. **72**, 4001 (1994).
[21] S. Steiner, S. Khmelevskyi, M. Marsmann, and G. Kresse, Phys. Rev. B **93**, 224425 (2016).
[22] B. Heinrich, Z. Celinski, J. F. Cochran, W. B. Muir, J. Rudd, Q. M. Zhong, A. S. Arrott, K. Myrtle, and J. Kirschner, Phys. Rev. Lett. **64**, 673 (1990).
[23] P. LeClair, H. J. M. Swagten, J. T. Kohlhepp, R. J. M. van de Veerdonk, and W. J. M. de Jounge, Phys. Rev. Lett. **84**, 2933 (2000).
[24] D. Kerkmann, D. Pescia, J. W. Krewer, and E. Vescovo, Z. Phys. B **85**, 311 (1991).
[25] M. P. Seah and W. A. Dench, Surf. Interface Anal. **1**, 2 (1979).
[26] Y. Nagai, T. Chiba, Z. Tang, T. Akahane, T. Kanai, M. Hasegawa, M. Takenaka, and E. Kuramoto, Phys. Rev. Lett. **87**, 176402 (2001).
[27] T.-C. Chiang, Surf. Sci. Rep. **39**, 181 (2000).
[28] J. M. An, D. Raczkowski, Y. Z. Wu, C. Y. Won, L. W. Wang, A. Canning, M. A. Van Hove, E. Rotenberg, and Z. Q. Qiu, Phys. Rev. B **68**, 045419 (2003).
[29] P. Heimann, J. Hermanson, H. Miosga, and H. Neddermeyer, Phys. Rev. B **20**, 3059 (1979).
[30] C. Carbone, E. Vescovo, O. Rader, W. Gudat, and W. Eberhardt, Phys. Rev. Lett. **71**, 2805 (1993).
[31] J. L. Bao, L. Galiardi, and D. G. Truhlar, J. Phys. Chem. Lett. **9**, 2353 (2018).
[32] W. J. Kim, S. Xing, G. Kremer, M. Sicot, B. Kierren, D. Malterre, G. Contini, J. Rault, P. Le Fèvre, F. Bertran, D. Rocca, Y. Fagot-Revurat, and S. Lebègue, J. Phys. Chem. C **123**, 26309 (2019).

All articles published on e-J. Surf. Sci. Nanotechnol. are licensed under the Creative Commons Attribution 4.0 International (CC BY 4.0). You are free to copy and redistribute articles in any medium or format and also free to remix, transform, and build upon articles for any purpose (including a commercial use) as long as you give appropriate credit to the original source and provide a link to the Creative Commons (CC) license. If you modify the material, you must indicate changes in a proper way.

Copyright: ©2026 The author(s)
Published by The Japan Society of Vacuum and Surface Science